Available online at www.sciencedirect.com
ScienceDirect
Tectonophysics 424 (2006) 41–51
TECTONOPHYSICS
www.elsevier.com/locate/tecto

Probing the history of the Mathematician paleoplate using surface waves

Yu J. Gu

Department of Physics, University of Alberta, Edmonton, Alberta, Canada T6G2J1

Received 25 December 2005; received in revised form 18 May 2006; accepted 2 June 2006
Available online 9 August 2006

Abstract

This paper investigates the shear velocity structure under the northern East Pacific Rise at the latitude range of 9–18°N, using intermediate-period Rayleigh and Love waves. The selected ocean-bottom seismic records provide source–receiver paths that ideally constrain the lithospheric mantle structure beneath the southern Rivera plate and the Mathematician paleoplate. The Rayleigh wave data infer a relatively thin (~30 km) lithosphere under the eastern side of the present-day East Pacific Rise. The associated shear velocities are consistent with existing models of oceanic mantle beneath this region, and the estimated plate age of 2–3 million years agrees with results from magnetic dating. The west of the rise axis is characterized by a thicker and faster lithosphere than the eastern flank, and such structural differences suggest the presence of a relatively old Mathematician paleoplate. The discontinuous change in mantle structure across the East Pacific Rise spreading center are observed in both isotropic and anisotropic velocities. The young oceanic lithosphere east of the rise axis shows strong polarization anisotropy, where the dominant orientation of crystallographic axes roughly parallels the spreading direction. However, the western flank of the rise axis is approximately isotropic, and the lack of anisotropy suggests complex deformation mechanisms associated with earlier episodes of ridge segmentation, propagation and dual-spreading on and around the Mathematician paleoplate.

Keywords: Mathematician paleoplate; East Pacific Rise; Love wave; Rayleigh wave; Shear velocity; Seismic anisotropy; Lithosphere; Low velocity zone

1. Introduction

Transfer of active spreading centers from one location to another generally occurs as an aftermath of plate boundary adjustment through ridge jumps and reorientation of ridge propagation directions. Prior to the eventual abandonment of the old ridge segments, two or more nearly parallel spreading centers could co-exist and, depending on the geometry of the ridge–ridge interaction, trap the lithosphere between them and thereby produce oceanic microplates. Over time, these microplates can potentially evolve into paleoplates long after the cessation of spreading at one or both of the competing ridges. Hence, the combination of "dual spreading" (Mammerickx et al., 1988) and the subsequent abandonment of a key component of the ridge–ridge interaction, due to continuous or discontinuous plate boundary readjustments (e.g., Hey, 1979; Klitgord and Mammerickx, 1982; Lonsdale, 1995), can be effective means to form paleoplates.

The aforementioned plate boundary processes could play a key role in the evolution of the Mathematician paleoplate west of the present-day northern East Pacific

E-mail address: jgu@phys.ualberta.ca.

0040-1951/$ - see front matter © 2006 Elsevier B.V. All rights reserved.
doi:10.1016/j.tecto.2006.06.002

Rise (from here on, EPR) ridge system. Bounded by the Rivera Fracture zone (north), the West O'Gorman fracture zone (south) and the EPR (east), the Mathematician paleoplate was strongly influenced by the Pacific–Farallon spreading and convergence at the west coast of the Americas (Klitgord and Mammerickx, 1982; Mammerickx et al., 1988; Lonsdale, 1995; DeMets and Traylen, 2000). Through seafloor spreading and subduction, parts or even entire ridge segments on the once-active Mathematician microplate have been created or abandoned (Macdonald et al., 1992). As the consequences of such adjustments, part of ridge undergoes spatially discontinuous jumps over distances from a few kilometers to over a hundred kilometers. Such jumps have been well documented by seafloor topographic, magnetic and side-scan sonar data (Lonsdale, 1985; Searle, 1989; Hey et al., 1989; Macdonald et al., 1992; Lonsdale, 1995), as have their direct imprints on the tectonic evolution of the region. The wide spectrum of seafloor-spreading rates varies from 7 cm/year north of the Clipperton fracture zone to about 13 cm/year near the Galapagos triple junction (e.g., DeMets and Stein, 1990), reflecting the complex tectonic history of dynamics in this region.

While the magnetic, topographic, and active source data place strong constraints on the northern EPR system, magnetic data suffer from the lack of spatial resolution and topographic/side-scan sonar data are limited to structures at relatively shallow depths. Broadband, passive seismic experiments using ocean-bottom seismometers (OBS) offer a viable alternative, with high lateral and depth resolutions on structures at both crust and mantle depths. In 1995, a team led by S. Webb conducted a small-scale OBS experiment called "Temporal Observation of Eruption Seismicity" (TOES), aiming at improving the overall understanding of the nature of the mantle beneath the northeastern Pacific. During this 6-month deployment, six OBS were positioned south of Clipperton Fracture Zone (~9°50′N) along the EPR and recorded several Mw>5 regional earthquakes that span the eastern and southeastern Pacific oceans. The diverse spatial sampling led to a recent study of temperature and melt content across the different ridge segments (Gu et al., 2005) that identified a high-velocity lithosphere (or lid) west of the present-day EPR axial rifts. The path-averaged Rayleigh-wave phase velocities provided preliminary constraints on the presence and effect of the Mathematician paleoplate.

This study furthers the Gu et al. (2005) analysis by providing (1) improved Rayleigh wave models, (2) qualitative error estimates, and (3) Love wave models that reveal the extent of anisotropy. The analysis in the subsequent sections highlights the substantial difference between the eastern and the western flanks of the present-day northern EPR. The Rayleigh and Love wave velocities both support a relatively normal ridge mantle beneath the eastern flank of the EPR and an older, entrapped lithosphere beneath the western flank of the ridge, as one would expect from a paleoplate. The lack of Love–Rayleigh anisotropy west of the EPR also suggests complexities in the tectonic history of the Mathematician paleoplate region.

2. Data and methods

This study focuses on the Rayleigh and Love waves generated by two earthquakes: (1) a Rivera Fracture Zone event with a strike-slip type focal mechanism and a source–receiver path that samples the Pacific side of the ridge axis, and (2) a subduction zone event near Guerrero, Mexico where the associated surface waves traverse the Cocos Plate (Fig. 1). For simplicity I will refer to them as event 1 (west of EPR) and event 2 (east of EPR) hereafter. The two event–station pairs are ideal for a direct comparison as they have nearly identical path lengths and distances from the axial rift. The seafloor bathymetric map in Fig. 1 (ETOPO5 database, Mueller et al., 1997) highlights the major fracture zones and topographic variations, among which the dormant Mathematician ridge is only visible by a series of juxtaposed, north–south trending topographic lows near 111°W.

Intermediate-period surface waves were analyzed for multiple stations, but a greater weight is assigned to a designated station that exhibits superior signal-to-noise ratios for both earthquakes (see discussions of multipathing in Section 3). The bulk of the surface wave energy from these two moderate-sized earthquakes is concentrated between 0.02 and 0.1 Hz, though appreciable amplitudes can be identified at most frequencies above 0.01 Hz. Fig. 2 shows a series of filtered vertical-component records with the corresponding corner frequencies specified next to each seismogram. The primary frequency range examined in this study is [0.03, 0.07 Hz], from which the final waveform is effectively a superposition of the filtered surface-wave wavelets that are sensitive to the upper 15–60 km (shaded region, Fig. 2).

The waveform modeling approach is similar to that used by Gu et al. (2005), which depends both on earthquake source mechanisms and on the elastic properties of the crust and mantle. I use Harvard CMT solutions (Dziewonski et al., 1981), obtained from global records of surface and body waves, to account for excitation at the source; solutions for both events are consistent with the expected fault orientations and plate motions. Earthquake depths and scalar moments were pre-determined by body-to-surface wave amplitude ratios (see Gu et al.,

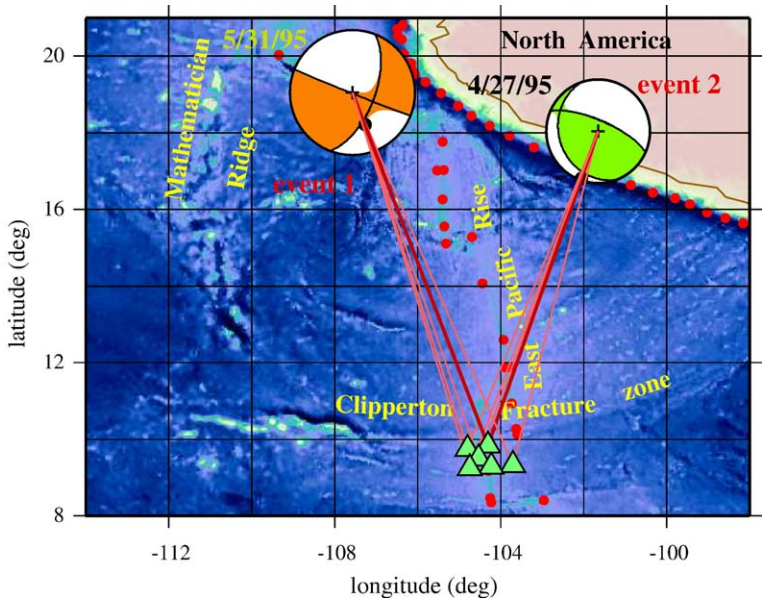

Fig. 1. Earthquake and station locations plotted onto a bathymetric map (Mueller et al., 1997) of the study region. The source mechanisms are taken from the Harvard CMT catalogue. Five out of six available stations are used in the Rayleigh wave analysis and only the one station is used in the Love wave analysis. The ray paths to the selected station are highlighted by the thick red lines.

2005), and they are well supported by the surface waves used in this study. The improved depth estimates of 9 km (Rivera fracture zone earthquake) and 60 km (Mexican Earthquake) help preserve the amplitude ratios computed from the OBS data.

The main objective of this study is to delineate the shallow mantle structure along the earthquake–station paths through forward modeling and inversion. First, synthetic seismograms are computed for laterally homogeneous, layered models with a modified reflectivity method (Fuchs and Muller, 1971; Kind, 1978; Herrmann and Wang, 1985) that incorporates a water layer (Xu and Wiens, 1997). Then, I adopt a linearized inversion technique (Randall, 1994) to achieve an optimal match between data and model synthetics for the surface wave window. The starting models of P and S velocities and

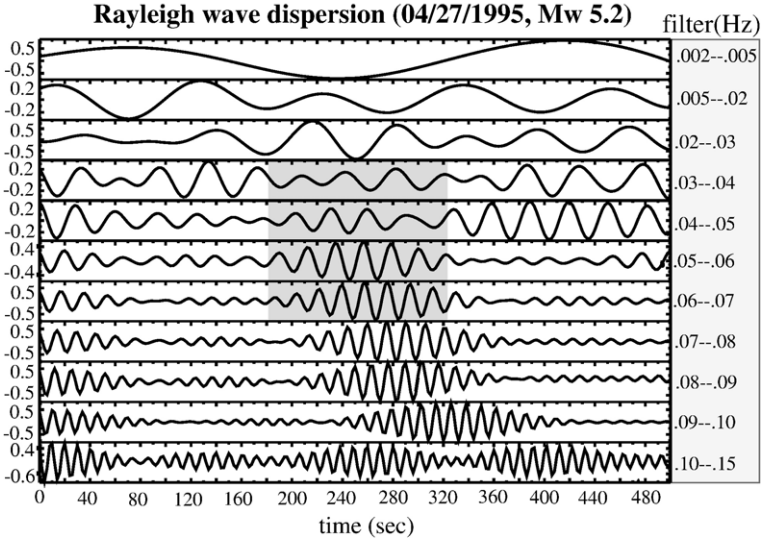

Fig. 2. Band-pass filtered vertical-component record of event 1 from a typical station. The values on the right-hand side of each seismogram denote the corner frequencies of the band-pass filter. Significant Rayleigh wave energy can be seen down to 0.02 Hz. The shaded area shows the Rayleigh wave phase window and the frequencies (from 0.03 to 0.06 Hz) considered by this study.

density have been previously obtained by Gu et al. (2005) from fitting vertical component OBS records. Through iterations, the combined forward and inverse approach improves the Rayleigh wave models from the earlier study and, for the first time, determines the Love wave models for the corresponding source–receiver pairs. Finally, quantitative measures of model errors are determined based on statistics (this study), rather than relying on empirical estimates (Gu et al., 2005).

3. Rayleigh wave models

Rayleigh wave phase velocities can be determined accurately owing to the high signal-to-noise ratios on the vertical-component OBS records. A comparison of the filtered data records and model predictions (Fig. 3) shows ~80% reduction to the original data variance. The visible difference in the estimated travel time curves for these two paths highlights the structural differences along the ray paths of this study. Smaller-scale lateral heterogeneities can be inferred from travel time variations among stations. For example, each data set contains at least one station with distinct phase velocities from the remaining records, mostly due to the strong effect of multi-pathing near the ridge axis where the station is located. Ideally, one could examine each earthquake–station pair and obtain a unique depth profile, but for the main purpose of contrasting velocity variations across the ridge I will focus on a station that is compatible with the majority of others. This station is used for both Rayleigh and Love wave analyses in order to minimize waveform dependencies on station site and instrument performance.

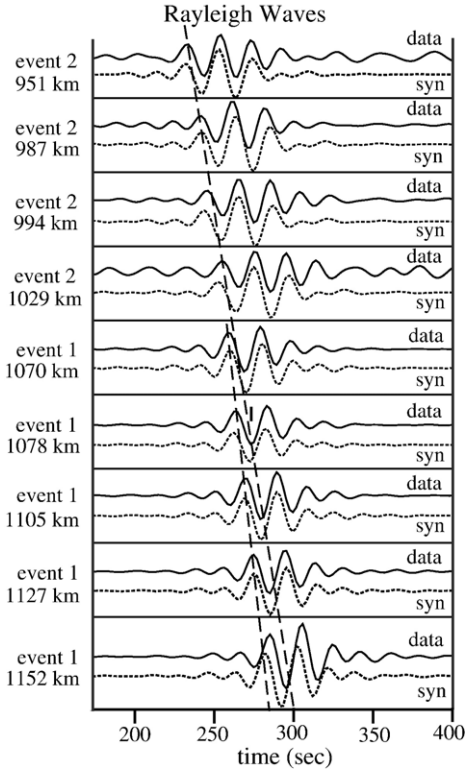

Fig. 3. Recorded and calculated Rayleigh waves for the two earthquakes analyzed in this study, shown in order by the solid and dotted curves. The two long-dashed lines track the approximate peaks of the first major swing in each phase group. The different slopes highlight the structural difference beneath the two paths. The Rayleigh waves are generally well matched by the theoretical waveforms computed using the best-fit shear velocity model.

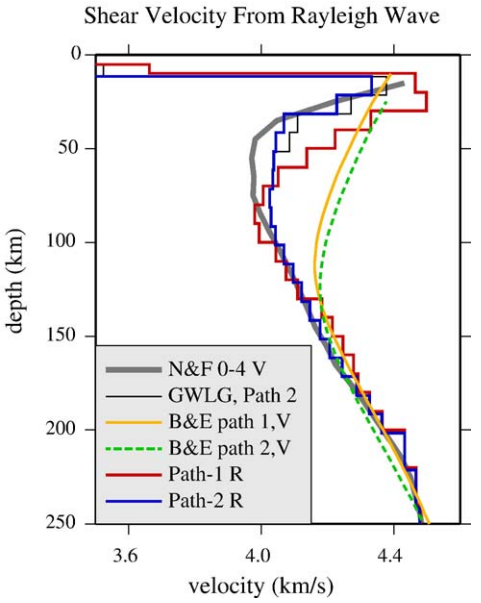

Fig. 4. SV-polarized and/or vertically propagating shear velocities obtained from Rayleigh waves. "N&F0–4 V" shows the "vertical velocity" (V_{SV}) model of Nishimura and Forsyth (1989) for a 0–4 Myr oceanic mantle. This model is obtained from an inversion of regional surface wave dispersion measurements for a transversely isotropic upper mantle. "GWLG path 2" (thin black line) was obtained by modeling the Rayleigh waves from path 2 (beneath the eastern flank of the EPR) by Gu et al. (2005). "B&E path 1, V" and "B&E path 2, V" represent the V_{SV} shear velocity model values of Boschi and Ekström (2002), averaged along path 1 and path 2, respectively. "Path-1 R" and "Path-2 R" show the respective best-fit models of the western and eastern flanks of EPR (this study) from Rayleigh wave phase velocities. The mantle structure east of EPR (Path-2 R) is reasonably consistent with N&F0–4 V model, but the western flank is characterized by a faster and thicker lithosphere and a relatively mild low velocity zone.

Fig. 4 compares the SV-polarized shear velocity obtained using Rayleigh waves generated by event/path 1 (red; from here on Path-1 R) and event/path 2 (blue; Path-2 R) with four existing models of the eastern Pacific. Path-1 R exhibits only marginal differences from an earlier model obtained by Gu et al. (2005) for the same

path; the latter model is not shown for simplicity. In comparison, the gray curve (see Fig. 4) shows the average "vertical velocity" (V_{SV}) model of Nishimura and Forsyth (1989) for ocean basins less than 4 million year old (from here on, NF0–4 V), determined for the entire Pacific region using regionalized surface wave dispersion measurements. Path-1 R contains a significantly faster (by ~4%) and thicker (by ~15 km) oceanic lithosphere than that predicted by NF0–4 V. Path-1 R also exhibits a strong low velocity zone underneath the lid, with minimum velocities falling below 4.0 km/s. The resulting steep velocity gradients associated with the lithosphere–asthenosphere transition appear to match the relative amplitudes of individual dispersive signals within the Rayleigh wave phase group.

The shear structure beneath the eastern side of the ridge (Path-2 R) is slightly slower than an earlier model of the corresponding path (Gu et al., 2005; labeled GWLG and represented by a thin black curve). Two factors could contribute to this modest difference. First, rather than finding an average structure that fits all available stations, this study places higher weight on a single representative station; second, this study uses Gu et al. (2005) model as the starting velocity and modest improvements were made to fit the waveform data after additional iterations. The overall characteristics of Path-2 R and NF0–4 V are consistent in the top 50 km, but both models are significantly slower than Path-1 R, the structure east of the ridge. The 0.12 km/s (~3%) overall difference between Path-2 R and Path-1 R cannot be reconciled by relatively minor fluctuations in data quality and plate age. In fact, the average path age between 1.5 Myr (west of the rise axis) and 2.3 Myr (east of rise axis) based on Mueller et al. (1997) should produce slightly slower velocities west of the present-day rise axis, but the opposite is observed.

The regional models described above generally show more pronounced low velocity zones than the path-averaged, vertical velocity (V_{SV}) of Boschi and Ekström, 2002 (labeled B&E path 1, V; see Fig. 4). This is not unexpected as the latter model was obtained from global inversions of surface waves from on-land stations. The lack of path coverage close to the ridge axis and the regularization/smoothing applied to the global inversions (e.g., Ekström and Dziewonski, 1998; Gu et al., 2005) could significantly reduce the overall amplitude of the velocity perturbations near spreading centers. The inherent difference between Rayleigh wave particle motions analyzed in this study and the so-called "vertical velocity", a shear velocity that depends on polarization as well as propagation direction, could also introduce some model differences. However, the effect due to the different definitions of shear velocity is likely secondary as both Nishimura and Forsyth (1989) and Boschi and Ekström (2002) inverted for transversely isotropic structures but produced the two end-member models in Fig. 4.

Formal uncertainties of the models are difficult to quantify because they depend on factors such as event mislocation and the choice of model parameterization. However, it is plausible to estimate the modeling error of shear velocities, particularly the lithosphere–asthenosphere velocity gradient, based on a statistical analysis of the reduction of data variance. I start with a candidate model and modify its lithosphere velocities by a uniform percentage to obtain a perturbed model. Then, a synthetic seismogram is calculated using the perturbed model and document the reduction to the original data variance in the selected Rayleigh wave window. I repeat this process for a suite of models that deviate (in lid

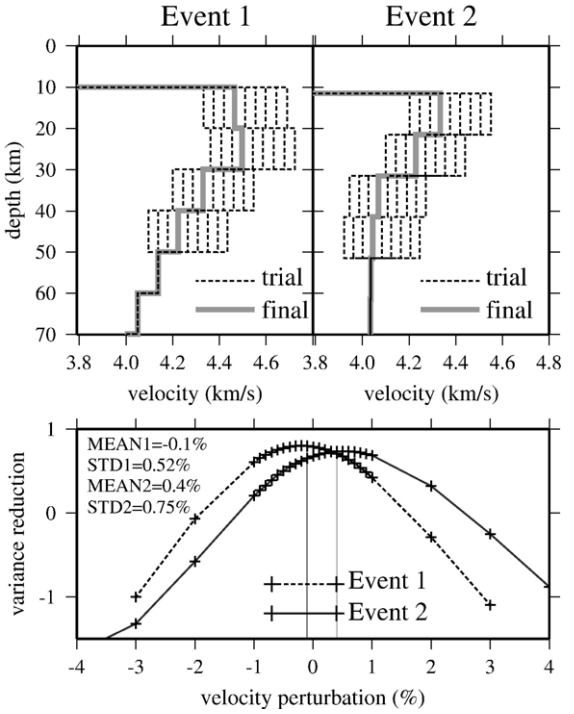

Fig. 5. A statistical estimate of model uncertainties in the Rayleigh wave analysis. In the top panel, the dotted lines represent a suite of trial 1D models (with 1% spacing) obtained by adding or subtracting a certain percentage of lithospheric velocity to/from the appropriate layers in the candidate model (solid gray curve). The bottom panel shows the associated variance reduction ("1" represents 100%) for the trial models. Smaller increment in model perturbations (0.1%) is taken between −1% and 1%. The variance reduction vs. model perturbation plot displays Gaussian-like distributions. The maxima in the total variance reduction of all available stations, as indicated by the two vertical lines, are close to the 0% perturbation that represents the original candidate models. The standard deviation of the distribution is used as a quantitative measure of model uncertainties.

velocity) from the candidate model by percentage values within [−4%, 4%] with 1% increment; finer perturbations are computed from −1% to 1%. By definition, a valid velocity model should fit the data well, such that a variance reduction versus percentage perturbation plot should approximately resemble a Gaussian distribution with ~0% mean perturbation. If so, the optimal model based on the distribution should be reasonably close to the candidate model (at 0% perturbation) and the standard deviation of the distribution can be an effective measure of model uncertainty.

By using the approach above I compute a suite of hypothetical, perturbed models based on the candidate models Path-1 R and Path-2 R (Fig. 5, top panel); the denser sampling between −1% and 1% is omitted for clarity. Fig. 5, bottom panel shows the variance reduction curves for the range of model perturbations in the lithosphere. For generality the variance reduction is calculated as the weighted sum of all available stations for a given event. The resulting distributions are approximately Gaussian. The standard deviations of the distributions are 0.52% for path 1 and 0.75% for path 2, which correspond to empirical model uncertainties of 1% or less for both lithospheric models. The optimal models (in view of variance reduction) are close to but not precisely positioned at the centers of the curves. This is, in part, a result of the subjective criterion to preferentially fit the Rayleigh waves at one station rather than all of the stations. The relatively small uncertainties for both paths could, at best, account for half of the observed model difference of 2.5% in their shallow mantle structures.

4. Love wave models

Love waves are harder to model since the horizontal-component records are strongly affected by lateral movements of ocean currents. More importantly, as an OBS descends to the ocean floor, the two horizontal components (north–south and east–west) undergo rigid-body rotations about the vertical axis and, therefore, the true orientation is unknown. I use a statistical analysis of the particle motion (e.g., Vidale, 1986; Toomey et al., 1998) to determine the station misorientation. First, I choose two large earthquakes (with bodywave magnitudes of 6.5 and 6.7) recorded by a designated station. The sense of particle motion is then recovered from the scatter plot of the two horizontal components for a selected Rayleigh wave window. Despite potential errors in recording and the presence of 3D heterogeneity and anisotropy, the time samples associated with a Rayleigh wave phase window should roughly follow a straight line oriented at a particular angle. Assuming Rayleigh waves have little or no energy on the transverse component, the station misorientation can then be determined by the orientation of the best-fit line through the scattered points. As the final step, I compare the polarity of P waves on the vertical and radial components after the rotation to determine if an additional 180° shift (or a sign change) is necessary. The resulting misorientation angles at the designated station are found to agree to 6–8° for the two selected earthquakes. These uncertainty values are consistent with those reported by Toomey et al. (1998), and are small enough to recover accurate models of shear velocities from Love waves. The average of the two angles is used as the final station misorientation and the appropriate rotation is subsequently applied to the horizontal components.

Love waves can be clearly identified on the transverse-component records after rotation (Fig. 6). I then perform the same forward and inverse modeling approaches outlined in the Section 3 to produce the best-fit Love wave model. The synthetic seismograms computed from the resulting models (see Fig. 6) closely match the observations, as both the amplitude and phase of the Love waves are successfully captured by the theoretical calculations. These models (Fig. 7; labeled "Path-1 L" and "Path-2 L") are compared with "horizontal" (or V_{SH}) velocity models of Nishimura and Forsyth (1989) (NF0–4 H; thick gray line) and Boschi and Ekström (2002) (B&E path 1, H and B&E path 2, H). For the latter study, the 1D velocity profiles are obtained by averaging the 3D V_{SH} model along the paths analyzed in this study.

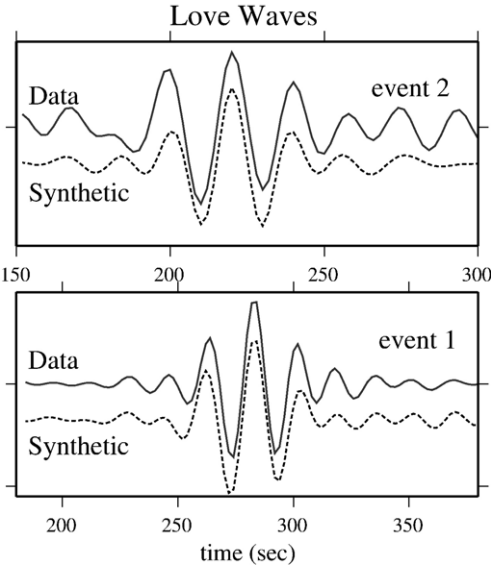

Fig. 6. Observed and model predicted Love waves on the transverse-component records. The final models from events 1 and 2 match the observations very well.

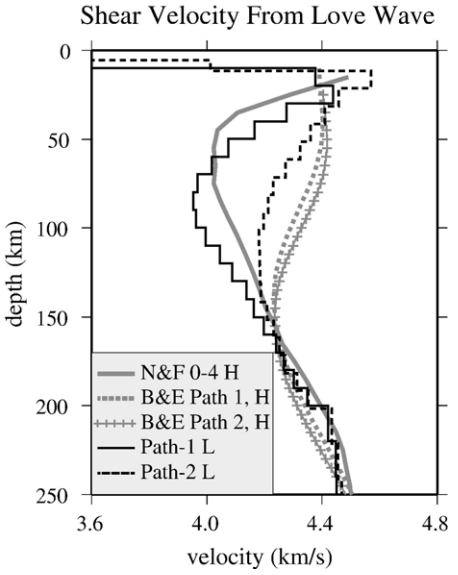

Fig. 7. A comparison of shear velocities obtained from the transverse-component records (this study) with existing "horizontal velocity" (V_{SH}) models that depends on wave particle motion as well as propagation direction. Model "N&F 0–4 H" represents the average V_{SH} model of Nishimura and Forsyth (1989) for a typical 0–4 Myr ridge mantle. The V_{SH} model values of Boschi and Ekström (2002; labeled "B&E") are obtained by averaging the horizontal shear velocities along the two source–receiver paths of this study. "Path-1 L" and "Path-2 L" represent the optimal Love wave models of this study for the eastern (path 2) and western (path 1) sides of EPR, respectively.

Path-1 L shows a lithosphere approximately 40–50 km thick, overlying a strong low velocity zone that potentially extends down to 80–100 km (see Fig. 7). The maximum lid velocity of ~4.35 km/s is slightly lower than the model value of N&F0–4 H (~4.4 km/s), but the velocity falloff with depth is less rapid than the latter model. The low velocity zone is ~1% slower and 15 km deeper than that shown by N&F0–4 H, but the overall characteristics of the two models are well correlated. In comparison with B&E (Boschi and Ekström, 2002), a 3D anisotropic model obtained by inversions of surface wave dispersion, the lid velocities match reasonably well but the low velocity zone velocities differ by 7% or more. In fact, model B&E H suggests a negative velocity gradient close to 100 km that could, to a certain degree, reflect the imperfect depth resolution of global models in general. Finally, a comparison of Figs. 4 and 6 shows that the main characteristics of Path-1 L, for example, a thick lid and a steep low velocity zone, are most consistent with the Path-1 R (obtained from Rayleigh waves) for the same path. This correlation could imply an effective isotropic mantle beneath path 1 (see Section 5 for further discussion).

The velocity profile east of the ridge axis (Path-2 L, see Fig. 7) is characterized by a high-velocity lid and an average velocity that exceeds 4.4 km/s. This value is marginally higher than the average lid velocity west of the ridge axis (~4.2 km/s). Underneath the lid, the model does not show a well-defined asthenospheric low-velocity zone, a distinct feature that contrasts sharply with Path-1 L. The overall asthenospheric velocity is slightly lower than the corresponding velocity exhibited by B&E H (for path 2), but it is substantially higher than that required by Love waves traveling on the western side of the ridge or by Rayleigh waves traveling on the same side of the ridge (see Figs. 4 and 7).

The model differences are clearly illustrated by the Love wave records in a series of hypothesis tests (Fig. 8). The top traces in each panel show the original Love wave record, and the bottom two traces show the predicted

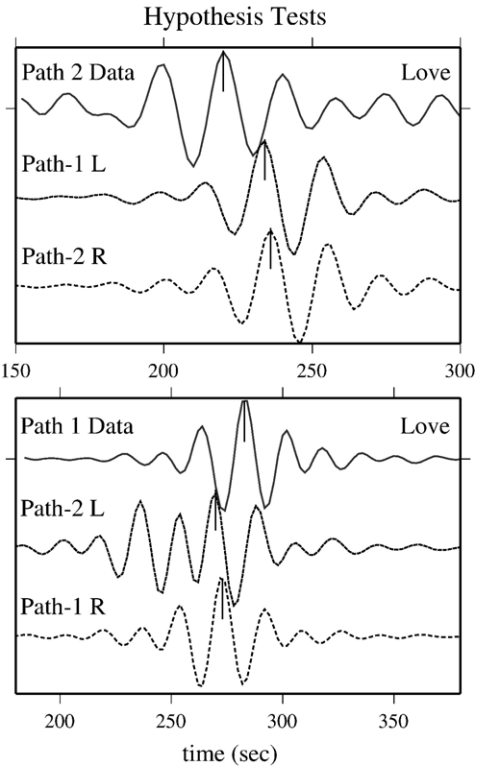

Fig. 8. Hypothesis tests of the final models using the Love wave records. The top traces in each panel show the observed Love waves for the two source–receiver paths. The middle traces represent a theoretical calculation of Love waves, assuming the same source and station information, using the Love wave model of the opposite side of the ridge axis. The bottom traces show predictions of Love waves using the SV-polarized velocity models of the same side of the ridge. Path 2 Love waves clearly demand a faster model than those tested, while path 1 Love waves arrive later than the "scrambled" model predictions.

Love wave arrivals using the SH-polarized model from the opposite side of the ridge (middle) and the SV-polarized model from the same side of the ridge (bottom), respectively. The event 2 Love wave observation, which reflects the transversely polarized structure east of the EPR axis, leads both model predictions by 10–15 s. This phase difference requires a much faster lid under the eastern flank of the EPR. Model differences are illustrated by path 1 Love wave data, as the observed waveform trails model predictions of Path-2 L and Path-1 R by 10 s or more.

Finally, I use the same statistical analysis described in Section 3 to quantify the model uncertainties. For both events, the waveform correlation between the synthetic and observed seismograms degrades quickly when the perturbed model moves away from the final models shown in Fig. 7. For example, if one increases the topmost lithospheric layer by 1% and decreases the underlying layer by 1%, the net change in velocity gradient can result a 10% decrease in variance reduction. The combined uncertainty in the two Love wave models is no larger than 3%, which at best accounts for half of the observed velocity difference of 7–8% between the two sides of the EPR. Hence, the observed east–west structural change is, most likely, physical. Uncertainties associated with earthquake depth, density and Q have only secondary effects on the phase velocities examined in this paper.

5. Discussion

The main results of this paper can be summarized by the strong changes in mantle seismic velocity and anisotropy across the present-day EPR rise axis in the latitude range of 9–18°N. These changes vividly reflect the complex plate boundary adjustments associated with the interaction of the Pacific, Mathematician, and Rivera plates in the last 10 Myr. The eastern flank of the present-day rise axis is considerably slower than the western side for a propagating Rayleigh wave sensitive to upper mantle depths. If we assume a simple conductive cooling model (e.g., Turcotte and Oxburgh, 1967; Forsyth, 1992; Carlson and Johnson, 1994) and a lid thickness of 35 km, the observed 4.2 km/s lid velocity would then correspond to a lithosphere age of 2–3 Myr and an approximate temperature of 1100 °C (Kato, 1997; Gu et al., 2005). This model-derived age is consistent with the 3.0–3.2 Myr by DeMets and Traylen (2000) from magnetic lineation and calculations of plate rotations. Furthermore, the relatively thin lid east of the EPR (~30 km thick), as evident in both SV-polarized (Path-2 R) and SH-polarized (Path-2 L) velocities, corroborates with the large-scale Rayleigh wave dispersion measurements of Nishimura and Forsyth (1989) for a 0–4 Myr ridge mantle. In short, the structure beneath the eastern flank of the present-day EPR represents a typical oceanic mantle near a fast spreading center.

The relative simplicity of the mantle beneath the eastern flank of EPR is also reflected by the presence of strong polarization anisotropy. The eastward ridge flow with a slight clock-wise rotation in recent history (DeMets and Traylen, 2000) appears to have strongly influenced the mantle fabric beneath this region. The SH-polarized velocity is more superior than SV-polarized velocity and the strength of anisotropy highlights the effect of finite strain which, based on recent results from mineral physics (Mainprice et al., 2000; Faul, 2001) and seismology (e.g., Nishimura and Forsyth, 1989; Ekström and Dziewonski, 1998; Levin et al., 1999; Montagner, 2002; Boschi and Ekström, 2002; Gung et al., 2003, 2005a), could cause a horizontal alignment of olivine a-axis at shallow mantle depths (Blackman et al., 1996). Ridge-normal flow could be a major cause of the finite strain that increases the velocity of Love waves traveling roughly southward; Rayleigh waves, on the other hand, prescribe to elliptical particle motions within planes that are normal to the flow lines. The amount of anisotropy we observe east of the EPR is larger than previously estimated (e.g., Nishimura and Forsyth, 1989; Ekström and Dziewonski, 1998). The difference could arise from differences in sampling: the path examined by this study represents a specific profile nearly parallel to the ridge axis (thereby sensing strong ridge effects), while the two earlier studies average over a much larger area using a diverse set of path azimuths, thereby slightly reducing the overall anisotropy.

The western side of the northern EPR, sampled by path 1, is significantly more complex. Based on marine seismic, topographical and magnetic data (e.g., Mammerickx et al., 1988; Macdonald et al., 1992; Canales et al., 2003), the Mathematician paleoplate was largely excluded from participating in the Wilson cycle (Fig. 9). This old plate largely maintains the tectonic imprints from past episodes of dual spreading and ridge jumps to the east. Additional complications such as the capture of littered lithospheric fragments from the Farallon plate (Mammerickx et al., 1988) may also affect the mantle signatures that we observe today. The formation of this paleoplate may have started when the failed Mathematician ridge, which was hypothesized to be the dominant mid-ocean ridge 10 million years (Myr) ago, gave way (at ~3 Ma) to a developing Moctozuma Trough (see Fig. 9) that eventually became part of the East Pacific Rise (DeMets and Stein, 1990). During the dual spreading episodes, the Mathematician paleoplate was sandwiched between the two spreading centers and lithosphere mantle is largely 6–10 Myr old, much older than eastern side of the present-day EPR.

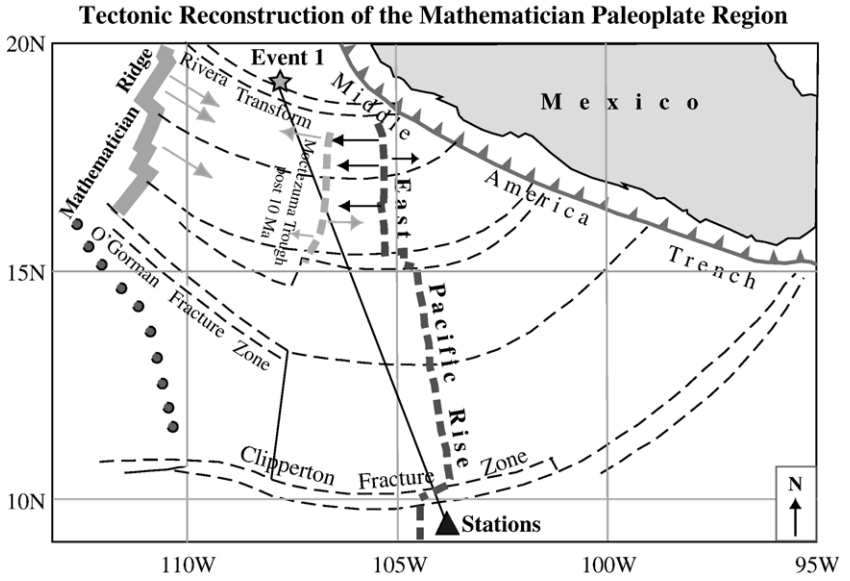

Fig. 9. Plate reconstruction of the Mathematician–Rivera–Pacific system (modeled after Mammerickx et al., 1988). The region bounded by the Mathematician Ridge, Rivera fracture zone, Moctezuma trough (EPR) and O'Gorman Fracture zone represents the Mathematician paleoplate. The light arrows show the past spreading directions of the Moctezuma Trough (which eventually evolved into the EPR) and of the dormant Mathematician ridge prior to the past 3 Myr; the solid arrows show the present-day spreading directions of the EPR. Episodic ridge jumps and dual-spreading occurred in the last 5–6 Myr.

Our OBS records west of the EPR suggest the presence of the Mathematician paleoplate. Path 1 directly samples this region from the source side and the resulting high Rayleigh wave model reflects a modified path age of ~5 Myr while assuming a lid thickness of 45 km (Kato, 1997; Gu et al., 2005). The long history of this region is further evidenced by a thick oceanic lithosphere of ~50 km, present in both Rayleigh and Love wave velocities. A strong low velocity zone inferred jointly from Rayleigh and Love waves suggests a deep-asthenospheric anomaly beneath the Mathematician paleoplate. It is not yet clear whether this anomaly represents a thermal origin or melt fraction beneath a relatively thick lithosphere. This asthenospheric feature is absent from the east of the EPR. The mantle structure imaged by SH-(Love) waves does not deviate significantly from the one obtained by SV-polarized (Rayleigh) waves; the agreement suggests an effectively isotropic mantle that may extend below 70 km. If the strength of anisotropy is any indication of "order" in the mantle (Anderson, 1989; Silver, 1996), the largely isotropic region west of the present-day EPR rise axis would signify a poorly ordered system with randomly distributed fast crystallographic axes, or, an ordered mantle with competing patches of vertically and horizontally aligned olivine crystals along the sampled ray path. The lack of strong radial anisotropy (or transverse isotropy) or the presence of significant azimuthal anisotropy could both lead to a seemingly isotropic mantle. Unfortunately, the effect of azimuthal anisotropy requires significantly more data to constrain (e.g., Montagner and Tanimoto, 1991).

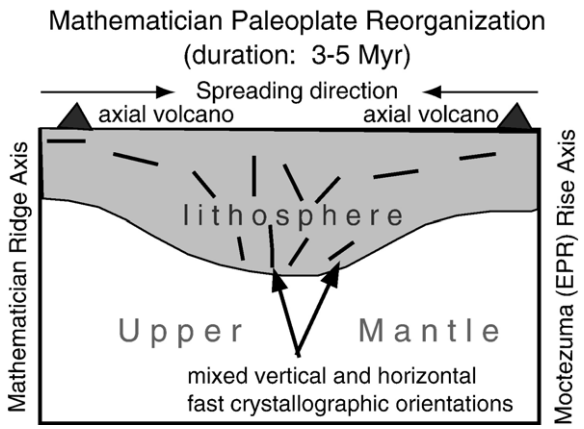

Fig. 10. A schematic diagram of changes in the potential mineral fast-axis orientations due to complex strain fields on and around the Mathematician paleoplate. Over a series of tectonic events such as ridge jumps and dual-spreading, the lithosphere underneath could undergo significant shortening (in the horizontal direction) and thickening (due to processes other than conductive cooling). The finite strain experienced in this region was quite complex and may explain the observed isotropic mantle beneath the eastern portion of the Mathematician paleoplate.

A suggested cause of isotropy west of the EPR is shown in Fig. 10. For the first 5–6 Myr, the oceanic lithosphere beneath the Mathematician paleoplate (at the time, a microplate) was assumed to contain strong transverse isotropy with a fast horizontal orientation, similar to the east of the present-day EPR and other young ocean basins near a fast-spreading ridge. The role of the captured Farallon plate lithosphere at this time is unclear, however. As the Moctezuma trough (the early EPR system) started to develop, the horizontal flow near the Mathematician ridge experienced major disruption due to a dual-spreading ridge system. The compressive stresses caused significant shortening in the east–west direction and extension in the north–south and vertical (depth) directions. Over the next 3–4 Myr, the deformation in this region became more complex, as the Mathematician paleoplate underwent episodic trench segmentation, migration and rotation. The initially ordered flow geometry and the associated horizontal anisotropy were largely diminished by the complex tectonic stresses over time (see Fig. 10). In particular, the vertical component of the strain field could cause the lineation direction of olivine crystals to rotate toward a vertical orientation. Consequently, the difference between SV and SH polarized velocities would become relatively small, a hypothesis that is well supported by the OBS data from event 1.

6. Conclusion

Overall, this paper shows two contrasting pictures of the lithospheric mantle beneath the two flanks of the northern EPR. The eastern side represents a young, fast-spreading ridge mantle that is characterized by relatively low Rayleigh wave velocities, a thin lid, and a significantly faster Love wave model due to flow-induced alignment of olivine crystals perpendicular to the north–south trending ridge segment. The western side of the EPR displays a faster, thicker lithosphere, consistent with an older oceanic lithosphere associated with the remnant of the Mathematician paleoplate. The mantle within the paleoplate is largely isotropic, resulting from the long history (~10 Myr) and the dual-spreading episodes of this region in the last 3–5 million years. The seismic observations presented in this study provide a small but valuable window into the dynamic history of the region. Though understandably with primarily two events recorded on the ocean floor, the spatial resolution remains an issue to be resolved in the near future. Hopefully, data from ongoing efforts such as the RIDGE2000 project can shed further light onto the formation and evolution of the northern East Pacific Rise ridge system.

Acknowledgements

I am grateful to Spahr Webb, Jim Gaherty and Art Lerner-Lam for providing the OBS data set and for extensive discussions of various issues related to this study. I sincerely thank Hans Thybo, Lapo Boschi and Vadim Levin for their careful reading and constructive suggestions. Thanks to Doug Toomey and students for providing their Matlab software for computing station misorientation angles, and to Keith Brzak and Curtis Dublanko for their comments during the preparation of this manuscript. Several of the figures are plotted using the GMT software (Wessel and Smith, 1991) and the data processing codes are partly based on the Seismic Analysis Code (SAC). This research is supported by NSERC, Alberta Ingenuity and the Canadian Foundation for Innovation (CFI).

References

Anderson, D.L., 1989. Theory of the Earth. Blackwell. 366 pp.

Blackman, D.K., Kendall, J.-M., Dawson, P.R., Wenk, H.-R., Boyce, D., Phipps Morgan, J., 1996. Teleseismic imaging of subaxial flow at mid-ocean ridges: traveltime effects of anisotropic mineral texture in the mantle. Geophys. J. Int. 127, 415–426.

Boschi, L., Ekström, G., 2002. New images of the Earth's upper mantle from measurements of surface wave phase velocity anomalies. J. Geophys. Res. 107, doi:10.1029/2000JB000059.

Canales, J.P., Detrick, R.S., Tommey, D.R., Wilcock, W.S.D., 2003. Segment scale variations in the crustal structure of 150–300 kyr old fast spreading oceanic crust (East Pacific Rise, 8–15N 10–5N) from wide angle seismic refraction profiles. Geophys. J. Int. 152, 766–794.

Carlson, R.L., Johnson, H.P., 1994. On modeling the thermal evolution of the oceanic upper mantle: an assessment of the cooling plate model. J. Geophys. Res. 99, 3201–3214.

DeMets, C., Stein, S., 1990. Present-day kinematics of the Rivera plate and implications for tectonics of southwestern Mexico. J. Geophys. Res. 95, 21 931–21 948.

DeMets, C., Traylen, S., 2000. Motion of the Rivera plate since 10 Ma relative to the Pacific and North American plates and the mantle. Tectonophysics 318, 119–159.

Dziewonski, A.M., Chou, T.-A., Woodhouse, J.H., 1981. Determination of earthquake source parameters from waveform data for studies of global and regional seismicity. J. Geophys. Res. 86, 2825–2852.

Ekström, G., Dziewonski, A.M., 1998. The unique anisotropy of the Pacific upper mantle. Nature 394, 168–172.

Forsyth, D.W., 1992. Geophysical constraints on mantle flow and melt generation beneath mid-ocean ridges. Mantle flow and melt generation at Mid-Ocean Ridges. Geophysical Monograph, vol. 71. AGU.

Faul, U.H., 2001. Melt retention and segregation beneath mid-ocean ridges. Nature 410, 920–923.

Fuchs, K., Muller, G., 1971. Computation of synthetic seismograms with the reflectivity method and comparison with observations. Geophys. J. R. Astron. Soc. 23, 417–433.

Gu, Y.J., Webb, S., Lerner-Lam, A., Gaherty, J.B., 2005. Upper mantle structure beneath the eastern Pacific Ocean ridges. J. Geophys. Res. 110, B06305, doi:10.1029/2004JB003381.

Gu, Y.J., Lerner-Lam, A., Dziewonski, A.M., Ekström, G., 2005. Deep structure and seismic anisotropy beneath the East Pacific Rise. Earth Planet. Sci. Lett. 232, 259–272.

Gung, Y., Panning, M., Romanowicz, B., 2003. Global anisotropy and the thickness of continents. Nature 422, 707–711.

Herrmann, R.B., Wang, C.Y., 1985. A comparison of synthetic seismograms. Bull. Seismol. Soc. Am. 75, 41–56.

Hey, R.N., 1979. Evidence for spreading center jumps from fine-scale bathymetry and magnetic anomalies near the Galapagos Islands. Geology 7, 504–506.

Hey, R.N., Sinton, J.M., Duennebier, F.K., 1989. Propagating rifts and spreading centers. In: Winterer, E.L., Hussong, D.M., Decker, R.W. (Eds.), The Geology of North America. The eastern Pacific Ocean and Hawaii, vol. N. Geological Society of America, Boulder, pp. 161–176.

Kato, M., 1997. An analysis of the temperature derivative of shear-wave velocity in the oceanic lithosphere of the Pacific Basin. J. Phys. Earth 45, 67–71.

Kind, R., 1978. The reflectivity method for a buried source. J. Geophys. 44, 603–612.

Klitgord, K.D., Mammerickx, J., 1982. Northern East Pacific Rise: magnetic anomaly and bathymetric framework. J. Geophys. Res. 87, 6725–6750.

Levin, V., Menke, W., Park, J., 1999. Splitting and relative delays of teleseismic shear waves in northern US. Seismol. Res. Lett. 70, 260.

Lonsdale, P., 1985. Linear volcanoes along the Pacific–Cocos plate boundary, 9 degrees N to the Galapagos triple junction. Tectonophysics 116, 255–279.

Lonsdale, P., 1995. Segmentation and disruption of the East Pacific Rise in the mouth of the Gulf of California. Mar. Geophys. Res. 17, 323–359.

Macdonald, K.C., Fox, P.J., Alexander, R.T., Pockalny, R., Gente, P., 1992. The East Pacific Rise and its flanks 8–18° N: history of segmentation, propagation and spreading direction based on SeaMARC II and sea beam studies. Mar. Geophys. Res. 14, 299–344.

Mainprice, D., Barruol, G., Ben Ismail, W., 2000. The seismic anisotropy of the Earth's mantle: from single crystal to polycrystal. Geophys. Monogr. 117, 237–264.

Mammerickx, J., Naar, D.F., Tyce, R.L., 1988. The Mathematician paleoplate. J. Geophys. Res. 93, 3025–3040.

Montagner, J.-P., 2002. Upper mantle low anisotropy channels below the Pacific Plate. Earth Planet. Sci. Lett. 202, 263–274.

Montagner, J.-P., Tanimoto, T.R., 1991. Global upper mantle tomography of seismic velocities and anisotropies. Geophys. Res. 96, 20 337–20 350.

Mueller, R.D., Roest, W.R., Royer, J.-Y., Gahagan, L.M., Sclater, J.G., 1997. A digital age map of the ocean floor, SIO Reference Series 93-30, Scripps Institution of Oceanography.

Nishimura, C.E., Forsyth, D.W., 1989. The anisotropic structure of the upper mantle in the Pacific. Geophys. J. R. Astron. Soc. 96, 203–229.

Randall, G.E., 1994. Efficient calculation of complete differential seismograms for laterally homogeneous Earth models. Geophys. J. Int. 118, 245–254.

Searle, R.C., 1989. Location and segmentation of the Cocos–Nazca spreading centre west of 95° W. Mar. Geophys. Res. 10, 41–57.

Toomey, D.R., Wilcock, W.S.D., Solomon, S.C., Hammond, W.C., Orcutt, J.A., 1998. Mantle seismic structure beneath the MELT region of the East Pacific Rise from P and S wave tomography. Science 280, 1224–1227.

Silver, P.G., 1996. Seismic anisotropy beneath the continents: probing the depths of geology. Annu. Rev. Earth Planet. Sci. 24, 385–432.

Turcotte, D.L., Oxburgh, E.R., 1967. Finite amplitude convective cells and continental drift. J. Fluid Mech. 28, 29–42.

Vidale, J.E., 1986. Complex polarization analysis of particle motion. Bull. Seismol. Soc. Am. 76, 1393–1405.

Wessel, P., Smith, W.H.F., 1991. Free software helps map and display data. Eos Trans. AGU 7, 445–446.

Xu, Y., Wiens, D.A., 1997. Upper mantle structure of the Southwest Pacific from regional waveform inversion. J. Geophys. Res. 102, 27 439–27 451.